UC Riverside
UC Riverside Previously Published Works

Title

Erythrocyte-derived photo-theranostic agents: hybrid nano-vesicles containing indocyanine green for near infrared imaging and therapeutic applications

Permalink

https://escholarship.org/uc/item/3h93c7nx

Journal

Scientific Reports, 3(1)

ISSN

2045-2322

Authors

Bahmani, Baharak
Bacon, Danielle
Anvari, Bahman

Publication Date

2013

DOI

10.1038/srep02180

Peer reviewed

OPEN

Erythrocyte-derived photo-theranostic agents: hybrid nano-vesicles containing indocyanine green for near infrared imaging and therapeutic applications

Baharak Bahmani, Danielle Bacon & Bahman Anvari

Department of Bioengineering, University of California, Riverside, Riverside, CA 92521 U.S.A.

Development of theranostic nano-constructs may enable diagnosis and treatment of diseases at high spatial resolution. Some key requirements for clinical translation of such constructs are that they must be non-toxic, non-immunogenic, biodegradable, with extended circulating lifetime. Cell-based structures, particularly those derived from erythrocytes, are promising candidate carrier systems to satisfy these requirements. One particular type of theranostic materials utilize light-sensitive agents that once photo-activated can provide diagnostic imaging capability, and elicit therapeutic effects. Here we demonstrate the first successful engineering of hybrid nano-scale constructs derived from membranes of hemoglobin-depleted erythrocytes that encapsulate the near infrared chromophore, indocyanine green. We show the utility of the constructs as photo-theranostic agents in fluorescence imaging and photothermal destruction of human cells. These erythrocyte-mimicking nano-structures can be derived autologously, and may have broad applications in personal nanomedicine ranging from imaging and photo-destruction of cancerous tissues to vascular abnormalities, and longitudinal evaluations of therapeutic interventions.

Transduction of light by specific molecules into other types of energy such as heat, chemical energy, and acoustic waves, has provided the basis for the development of photothermal therapy and photodynamic therapy (PDT) procedures, as well as diagnostic methods based on fluorescence and photoacoustic imaging. The use of near infrared (NIR) wavelengths (λ), particularly in the range of $\approx$650–1450 nm, is especially advantageous since in this "optically transparent window," light can penetrate relatively deeply into biological materials as there is minimal photons absorption by endogenous molecules[1].

Delivering NIR-transducing exogenous materials to a particular target of interest (e.g., abnormal vasculature, tumor mass) provides an approach to enhance the local optical absorption of the target. Once activated by NIR light, the exogenous material may be used as a photo-theranostic agent to enhance both the optical contrast of the target, and phototherapeutic efficacy, particularly in deeply seated targets.

A particular NIR-transducing molecule is Indocyanine Green (ICG) ($C_{43}H_{47}N_2NaO_6S_2$; molecular weight $\approx$ 775 Da). It is composed of two polycyclic (benzoindotricarbocyanine) lipophilic moieties, linked with a polyene bridge. A sulfonate group, bound to the nitrogens of each polycyclic part, provides net negative charge and water solubility. Therefore, the entire molecular structure leads to amphiphilic characteristics of ICG.

ICG's medical applications began in late 1950's for measurements of cardiovascular output to characterize valvular and septal defects[2], and soon after it was used to assess hepatic function[3]. It received supplemental approval by United Stated Food and Drug Administration (FDA) for ophthalmic angiography in 1975. In ophthalmological applications, ICG is recommended for imaging selective chorioretinal disorders including suspected polypoidal choroidal neovascularization (CNV), chronic central serous chorioretinopathy (CSC), and choroidal hemangioma[4]. To-date, ICG remains the only NIR dye approved by FDA for cardiocirculatory measurements, liver function tests, and ophthalmological imaging.

In addition to its current clinical utility, ICG has been investigated for sentinel lymph node mapping in patients with melanoma, prostate, breast, and other types of cancer[5–8]. Its utility in fluorescence-guided PDT of choroidal disease has also been reported[9,10]. Additionally, ICG has been studied for potential phototherapeutic applications including treatment of CSC[11], cutaneous hypervascular malformations[12], and PDT of choroidal melanoms[13].

Despite usage in clinical medicine, ICG's major drawbacks are its short half-life within plasma (≈2–4 minutes), and exclusive uptake by hepatic parenchymal cells followed by biliary excretion. Given its amphiphilic nature, ICG binds to various molecular species including albumin, and high- and low-density lipoproteins within the vasculature. Given these limitations, the potentials of this clinically-proven exogenous material as a theranostic agent for broader medical applications, which may require extended circulating lifetimes, remain limited.

Encapsulation has been investigated to shield ICG from non-specific interactions within the plasma, and extend its circulation time in the vasculature. Our group has reported that encapsulation of ICG into synthetic polymer-based nano-constructs enhances the contrast of *in vivo* fluorescent images from the heart and lungs for at least up to 90 minutes[14], and delays maximal hepatic accumulation to at least 60 minutes after tail vein injection in mice[15].

Recently, attention has been given to the use of biological materials as platforms for the delivery of therapeutic or imaging agents. We have reported the use of genome-depleted plant infecting brome mosaic virus doped with ICG as a nano-construct for NIR fluorescence and photoacoustic imaging[16,17].

Mammalian cells, particularly erythrocytes, present another type of biological vectors for the delivery of therapeutic and imaging agents[18–21]. In relation to cell-based imaging, hemoglobin-depleted red blood cells (erythrocyte ghosts (EGs)) have been used to encapsulate iron oxide for potential magnetic resonance imaging (MRI) applications[22–24]. Gold nanoparticles have been incorporated into human erythrocytes to produce tracers with enhanced contrast for potential dynamic X-ray imaging of blood flow[25]. Fluorescein isothiocyanate, a *non*-NIR dye, has been successfully loaded into EGs having diameters of ≈5 μm, with the intention of developing such constructs as plasma analyte or extracellular pH sensors[26,27]. Flower *et al.* recently loaded ICG into micron-sized EGs, and utilized the constructs as a fluorescent analogue of erythrocytes to characterize the movement of erythrocytes in retinal capillaries and choriocapillaris of monkeys and rabbits[28].

Here, we report the first proof-of-principle to demonstrate the successful engineering of ICG-loaded *nano-sized* vesicles derived from EGs, and their utility as photo-theranostic agents for fluorescence imaging and photothermal destruction of cells. We refer to these nano-vesicles as <u>n</u>ear infrared <u>e</u>rythrocyte-mimicking <u>t</u>ransducers (NETs).

Results

We can manipulate the diameter distribution of the NETs, and subsequently, their photophysical properties by varying the extrusion procedures required to fabricate nano-sized constructs, and the time of the EGs exposure to the hypotonic solution containing ICG at a given concentration. With the exception of the transmission electron microscope (TEM) image of the NETs, all results presented herein are based on 20 initial extrusions of EGs through 400 nm diameter polycarbonate porous membranes, followed by 20 additional extrusions through 100 nm diameter membranes, subsequent addition of 215 μM ICG into the hypotonic buffer solution containing the suspension of the nano-sized EGs, and incubation for five minutes (see Supplemental Information for effects of incubation time on diameter distribution, absorption, and loading efficiency).

The measured peak (d_{peak}) and estimated mean ($\bar{d}_{mean}$) diameters of EGs are 80.77 nm and 95.26 nm, respectively (Figure 1a). When doped with ICG, d_{peak} and $\bar{d}_{mean}$ increase to 134.78 nm and 124.61 nm, respectively. Only about 5% of ICG leaks from the NETs after one hour (see Supplemental Information).

Transmission electron microscope (TEM) imaging confirms the nano-sized diameter of the NETs (Figure 1b). NETs imaged by TEM were fabricated by six extrusions through 100 nm membranes, and using 215 μM ICG.
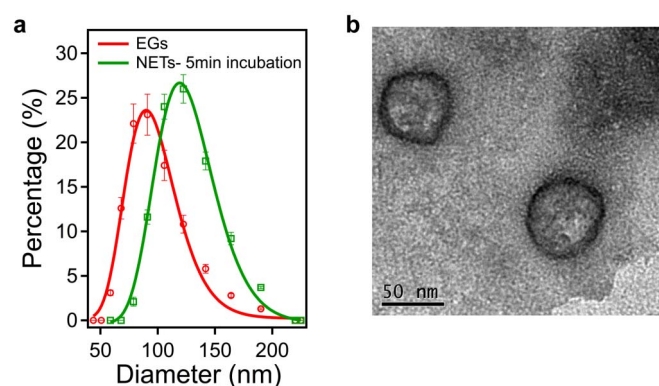

Figure 1 | Size distribution profiling and TEM image of NETs.
(a), Diameter distributions of EGs and NETs. Using dynamic light scattering, the ranges of the measured diameters are 58–190 nm for the EGs, and 78–190 nm for the NETs formed after five minutes of incubation in hypotonic solution and PBS containing 215 μM ICG. Each measurement was repeated using at least three samples. We present the mean of each measurement, represented as circles for EGs, and squares for NET. The error bars represent standard deviations from the mean values. We fitted Lognormal functions to the measured diameter distributions (solid curves). The estimated mean diameters, as determined by the Lognormal fits, are 95.26 nm ($R^2 = 0.97$), and 124.61 nm ($R^2 = 0.98$) for EGs and NETs, respectively. (b), Illustrative TEM image of NETs.

Absorption spectrum confirms the elimination of EG's hemoglobin content as evidenced by the absence of the signature absorption peaks of oxygenized hemoglobin at 542 and 576 nm, and that of deoxygenized hemoglobin at 556 nm (Figure 2a). The UV absorption for both non-loaded EGs and NETs is attributed to membrane proteins. Doping the EGs with ICG endows the constructs with NIR absorption capability.

The absorption spectrum of free ICG consists of spectral peaks at 780 and 707 nm, corresponding to the monomeric and dimeric (H-like aggregate) forms of ICG (Figure 2a), consistent with the well-established spectra of diluted (μM level) ICG in distilled water[29]. In comparison to free ICG, the absorption spectrum of NETs has several differences: (1) increased absorbance values for $\lambda > 600$ nm, explained by the fact that higher ICG concentration was used to fabricate the NETs; (2) elimination of the previously distinct absorption peak associated with the H-like aggregate form of free ICG at 707 nm; (3) broadened absorption spectrum over the 600–935 nm band; and (4) bathochromic (red) shift from 780 to 783 nm (with respect to the spectral peak associated with the monomer form of ICG). We attribute these differences to the presence of various conformational states of ICG, and induced changes in molecular dipoles and polarizability of ICG when encapsulated into these constructs (Figure 2b). We offer further explanations in the discussion section.

The spectral peak of fluorescent emission from NETs in response to photo-excitation at 650 nm is at 695 nm , and originates from the aggregated forms of ICG within the constructs (Figure 3a). Spectral peaks of fluorescence for free 3.22 μM ICG in response to 650 nm excitation are at 695 nm and 793 nm, and correspond to the H-like aggregate and monomeric forms of ICG, respectively. Fluorescence emission of free ICG at the higher concentration of 43 μM is quenched, and resembles that of the EGs, which do not contain ICG. We summarize the spectral features of the NETs fabricated under the protocol reported here in Table 1.

Human dermal micorvascular endothelial (HDME) cells were incubated with NETs or free ICG for three hours, and subsequently washed twice with phosphate buffer saline (PBS) prior to fluorescent imaging induced by photo-excitation at 740 ± 35 nm spectral band provided by a Nikon Mercury/Xenon arc lamp. Co-registration of
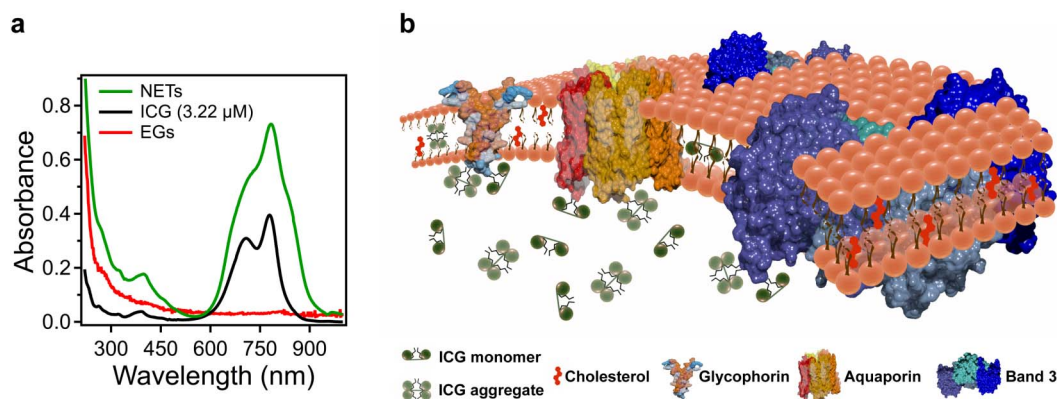
Figure 2 | Absorption spectra and a physical model of a NET containing ICG. (a), Absorption spectra corresponding to free (non-encapsulated) ICG (3.22 μM) dissolved in PBS, and EGs and NETs re-suspended in PBS after fabrication. (b), A physical model of a NET showing an ensemble of ICG conformational states comprised of ICG monomers, ICG aggregates, and monomers and aggregates of ICG bound to membrane lipids and/or membrane proteins. For illustration purposes, we present three main membrane integral proteins of erythrocytes: Aquaporin, Band3 and Glycophorin.

the NIR fluorescent emission from the constructs, and the visible fluoresce emitted by staining the nuclei of the cells produced images that suggest the NETs were internalized and localized to the nuclei periphery (Figure 3b). The maximum NIR emission intensity from HDME cells incubated with free ICG (Figure 3b, left panel) was ≈ eight times lower than that from the cells incubated with NETs (Figure 3b, right panel). This result indicates that free ICG was not effectively uptaken by the HDME cells since most of it was removed after washing the cells. However, cell wash was not as effective in removing the NETs, indicating that the uptake of the NETs by the HDME cells was greater than ICG uptake.

Temperature measurements indicate that NETs, suspended in PBS, are capable of eliciting a photothermal response in response to laser irradiation at 808 nm and incident intensity (I_o) of 19.7 W·cm^{-2} for 200 s (Figure 4a); however, sustained laser irradiation was accompanied by a reduction in temperature. Since these temperature measurements were made 2.0 mm away from the laser irradiated spots, they actually underestimate the true temperature of the NETs or ICG in response to laser irradiation. Nevertheless, these

suggests that ICG within the NETs can be photo-degraded (see Supplemental Information for the effect of cyclic laser irradiation on temperature). To further investigate the photostability of the NETs, we obtained the absorption spectra of the NETs following laser irradiation at 808 nm and I_o = 19.7 W·cm^{-2} for different radiant exposure times (60 s–200 s). There was a progressive reduction in the absorption of NETs over the 630–950 nm spectral band, and increased UV absorption at 213 and 245 nm with increasing radiant exposure time (Figure 4b).

HDME cells were incubated with NETs or free ICG (positive control) for three hours, and subsequently washed twice with PBS prior to laser irradiation at 808 nm laser irradiation with I_o = 19.7 W·cm^{-2} for 200 s. Cells incubated in PBS without exposure to NETs or ICG were used as the negative control population. Live/dead assays demonstrate that NETs are capable of mediating photothermal destruction of the HDME cells (Figure 4c). There was a statistically significant difference ($p < 10^{-4}$) between the fraction of photo-thermally destroyed HDME cells after three hours of incubation with NETs, and those incubated with free ICG or PBS
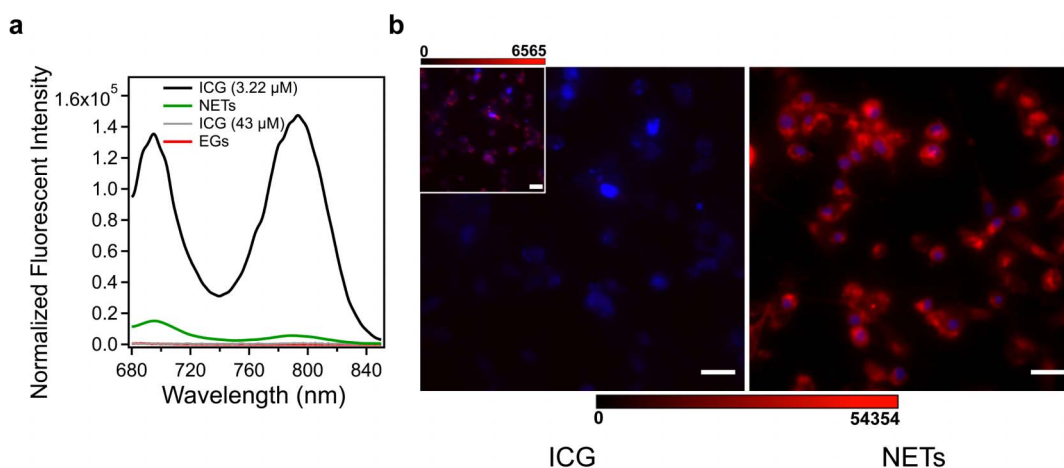

Figure 3 | Fluorescence spectra and fluorescent images of human dermal microvascular endothelial (HDME) cells incubated with ICG or NETs. (a), Normalized fluorescence spectra in response to 650 nm photo-excitation of free ICG (3.22 and 43 μM) dissolved in PBS, and EGs and NETs re-suspended in PBS. Emission spectra were smoothed using IGOR Pro software with second order binominal algorithm. (b), Fluorescent images of HDME cells after three hours of incubation in vascular cell basal medium containing 13 μM ICG (control) dissolved in PBS (left panel), or NETs (right panel) at 37°C and 5% CO$_2$ in dark. A Mercury/Xenon arc lamp was used for photo-excitation at 740 ± 35 nm. Cells nuclei were stained by DAPI, and falsely colored in blue using the ImageJ software. A filter transmitting $\lambda > 780$ nm was used to collect the emitted NIR fluorescent, falsely colored in red. Scale bars on both panels correspond to 10 μm. The scale bar, 0–54354, corresponds to the NIR fluorescent emission intensity for both panels. The inset on the left panel represents the same image shown on the panel at the scale of 0–6565.

Table 1 | Spectral Features of 3.2 μM free ICG, and NETs* in PBS

Feature	Wavelength (nm)
Absorption peak of monomers in free ICG	780
Absorption peak of ICG monomers in NETs	783
Absorption peak of dimers (H-like aggregates) in free ICG	707
Absorption peak of dimers (H-like aggregates) in NETs	Not distinct
Fluorescence peak of monomers in free ICG (650 nm excitation)	793
Fluorescence peak of monomers in NETs (650 nm excitation)	790
Fluorescence peak of dimers (H-like aggregates) in free ICG (650 nm excitation)	695
Fluorescence peak of dimers (H-like aggregates) in NETs (650 nm excitation)	695

*The spectral features of the NETs correspond to the constructs fabricated by 20 initial extrusions of EGs through 400 nm diameter porous membranes followed by 20 additional extrusions through 100 nm diameter membranes, using 215 μM ICG in hypotonic buffer solution, and five minutes of incubating the EGs with ICG.

(Figure 4d). The results presented in Figures 3b, 4c, and 4d collectively demonstrate the effectiveness of NETs as photo-theranostic agents for combined fluorescence imaging and photothermal destruction.

To evaluate the potential cytotoxicity of the NETs, we incubated the HDME cells for three and 24 hours in the culture medium containing the NETs at effective dosage (D_{eff}) of 12 ml^{-1} suspended in PBS (see Methods section for definition of D_{eff}). Nearly all the HDME cells remained viable after three hours of incubation with NETs at $D_{eff} = 12$ ml^{-1} (Figure 5a). After 24 hours of incubating the HDME cells with NETs at $D_{eff} = 12$ ml^{-1}, nearly 80% of the cells remained viable. In comparison, there was more than 90% cell death

following 24 hours of incubation with methanol as the positive control. Illustrative fluorescent image of the HDME cells demonstrate the viability of most of the cells after 24 hours of incubation with NETs at $D_{eff} = 12$ ml^{-1} (Figure 5b).

Discussion

Spectral broadening of the NETs absorption, and the elimination of a distinct dimeric (H-like aggregate) peak are indicative of different conformations of ICG. Specifically, when ICG is incorporated into the EGs, an ensemble of ICG conformational states comprised of ICG monomers, ICG aggregates, and monomers and aggregates of ICG bound to membrane lipids and/or membrane proteins can form
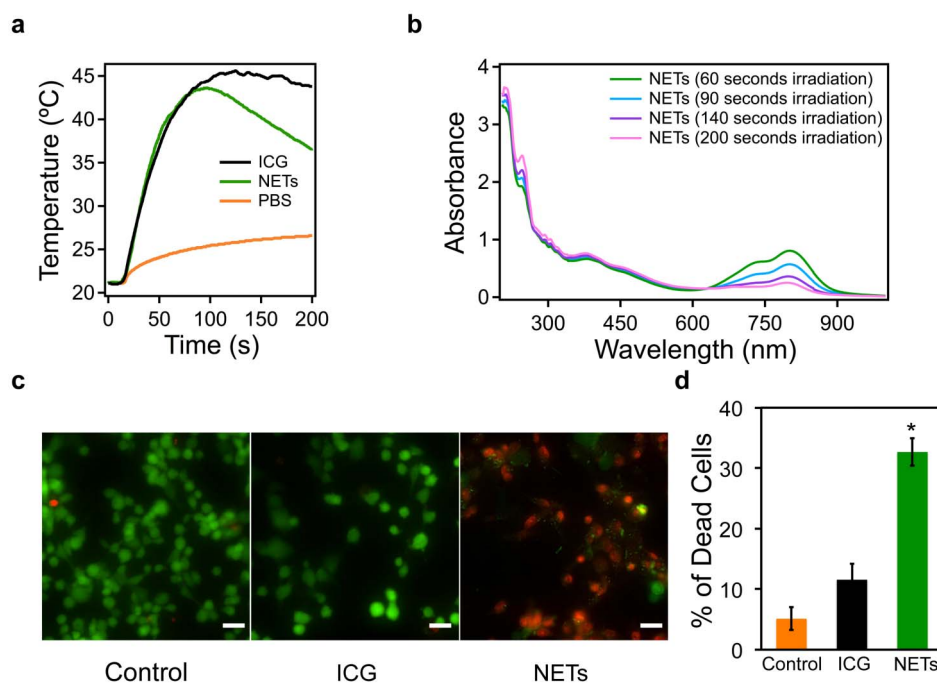

Figure 4 | Photothermal response of NETs, and NETs-mediated photothermal destruction of HDME cells. (a), Photothermal response of NETs suspended in PBS, 13 μM free ICG dissolved in PBS (positive control), and PBS solution (negative control) in response to laser irradiation at $\lambda = 808$ nm with incident intensity (I_o) of 19.7 W·cm^{-2}. The volume of all samples was 120 μl. The free ICG solution and NETs suspension samples were prepared to have nearly the same absorbance value of 0.6 at 808 nm. Temperatures were measured using a thermistor placed 2 mm outside the irradiated spot. (b), absorption spectra of four different PBS-suspended NETs samples (each 120 μl) following laser irradiation for various durations (60, 90, 140, and 200 s) at 808 nm and $I_o = 19.7$ W/cm^2. (c), Fluorescent images of HDME cells after three hours of incubation with PBS (negative control), 13 μM free ICG (positive control) and NETs, followed by laser irradiation ($\lambda = 808$ nm, $I_o =$ of 19.7 W·cm^{-2}).The radiant exposure time in all three samples was 200 s. The volume of NETs suspension or free ICG added to the cells was 200 μl with nearly the same absorbance value of 0.6 at 808 nm. Live cells were stained using Calcein, and falsely colored in green. Dead cells were distinguished using Ethidium homodimer-1 (EthD-1), and falsely colored in red (Scale bars = 10 μm). (d), Percentage of HDME cells photothermally destroyed by NETs as assessed by a fluorescence microplate reader. Three different spots (each spot diameter = 2.2 mm) were irradiated in each well, resulting in irradiation of ≈80% of cells. Each bar represents the mean fraction of the dead cells for three different wells. Error bars correspond to single standard deviations. There was a statistically significant difference in fraction of cells photothermally destroyed by NETs (identified by the asterisk) as compared to those incubated in PBS or free ICG ($p < 10^{-4}$).
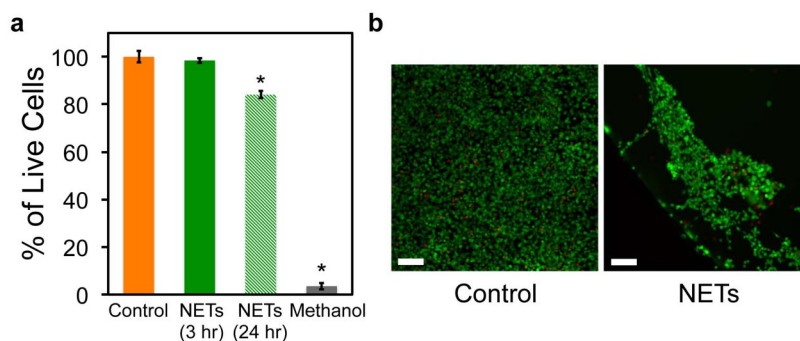
Figure 5 | Cytotoxicity assessment of NETs. (a), Percentage of live cells post incubation with NETs for 3 hours (solid green bar) and 24 hours (dashed green bar). Cells incubated with culture medium for 24 hours without any additional reagent were used as the positive control population. Cells incubated with 100 µl methanol for 24 hours were used as negative control. Each bar represents the mean fraction of the live cells for three different wells. Error bars correspond to single standard deviations. Statistical analysis of the results for NETs (3 hours) compared to positive control yielded no significant difference in cell viability. Cells treated with methanol (negative control) and NETs for 24 hours (identified by asterisks) yielded statistically significant viability results as compared to the positive control population ($p < 10^{-3}$). Fraction of the viable cells treated with NETs for 24 hours was significantly higher than those treated with methanol ($p < 10^{-4}$). (b), Fluorescent images of HDME cells 24 hours post incubation with NETs (right panel) and culture medium (positive control) (right panel). Live cells were stained using Calcein, and falsely colored in green. Dead cells were distinguished using Ethidium homodimer-1 (EthD-1), and falsely colored in red (Scale bars = 100 µm).

(Figure 2b). The excited energy levels associated with these ICG ensemble components, confined within the nano-scale volume of NETs, can be different than those associated with non-encapsulated (free) ICG. The effective NIR absorption cross section of the ensemble (σ_{ensemble}), which is directly related to NIR absorbance of the NETs, can be expressed as:

$$\sigma_{\text{ensemble}}(\lambda) = f_M \sigma_M(\lambda) + f_A \sigma_A(\lambda) + \sum_{i=1}^{n} f_{M_i^B} \sigma_{M_i^B}(\lambda) + \sum_{i=1}^{n} f_{A_i^B} \sigma_{A_i^B}(\lambda) \tag{1}$$

where f_M and f_A are the respective fractions of the monomeric and aggregated forms of ICG in the ensemble; σ_M and σ_A are the absorption cross sections of the monomeric and aggregated forms of ICG respectively; $f_{M_i^B}$ and $f_{A_i^B}$ are the respective fractions of the ensemble comprised of the monomeric and aggregated forms of ICG bound to a given membrane-associated molecule (i); $\sigma_{M_i^B}$ and $\sigma_{A_i^B}$ are the absorption cross sections of the monomeric and aggregated forms of bound ICG, respectively.

The observed bathochromic shift of the monomer absorbance in NETs is indicative of the changes in molecular dipoles and polarizability of ICG. We use the exciton theory for molecular assemblies to explain the origin of this bathochromic shift[30]. In accordance with this theory, the excitonic state of the ICG monomer bound to membrane lipids or proteins can split into two levels (E'' and E'). The in-phase arrangement of transition dipoles leads to an electrostatic attraction that produces the lower excited state (E'). Photo-excitation of the bound monomer produces a transition from ground to E', resulting in a bathochromic shift for the bound ICG monomer. A similar bathochromic shift in the monomer absorbance is reported for ICG dissolved in aqueous solution containing human serum albumin, and attributed to the interaction between albumin and ICG[29].

Fluorescence spectra in response to photo-excitation at 650 nm demonstrate that the emission intensity at 790 nm, associated with the monomer form of ICG in NETs, is diminished in comparison with the emission intensity of 3.22 µM free ICG at 793 nm (Figure 3a). The 650 nm excitation wavelength does not correspond to the spectral peaks associated with the monomeric forms of ICG in its free form or in the NETs (Figure 2a). The fact that in response to 650 nm excitation, we still observed a distinct fluorescence emission peak at 793 nm from the monomeric form of 3.22 µM free ICG, which was more intense than that from the monomer form of ICG in NETs, suggests that the fraction of ICG in its aggregated form is

greater than its monomeric fraction within the NETs. However, in the 3.2 µM free ICG solution, there were sufficient number of monomers to elicit fluorescence emission.

While fluorescence is quenched in the case of 43 µM free ICG, NETs are still fluorescent despite the fact that they were fabricated using 215 µM ICG (with loading efficiency of 30% to give an effective loaded concentration of 64.5 µM distributed into the population of the constructs) (Figure 3a). This result suggests that the presence of the erythrocyte-derived membrane, as an encapsulating shell, protected the entrapped ICG molecules within each NET from interactions with other such entrapped ICG molecules to ultimately prevent fluorescence quenching. While ICG molecules still form aggregates within the NETs, the effective concentration of such aggregates within the NETs fabricated under the protocols described herein, was not sufficient to induce fluorescence quenching that would otherwise take place at high (e.g., 43 µM) concentrations of free ICG in solution. Therefore, by loading the ICG into the NETs, higher ICG concentrations that could otherwise results in fluorescence quenching of its free form, may be used. In our future studies, we will characterize the effects of ICG concentration over a broad range on the resulting excitation-emission spectra of the NETs and fluorescence quantum yields.

Continuous laser irradiation at the specific parameters investigated here can result in photo-degradation of the NETs (Figure 4b). The progressive increase in absorbance values at the spectral peaks of 213 and 244 nm with increased radiant exposure time is indicative of the conformational changes in the membrane proteins of the NETs due to photothermal denaturation. Our observed progression in reduction of the NET's NIR absorption with sustained laser irradiation can result from photo-addition to the alternating double bonds in the polyene bridge of the ICG molecule to produce a leuco form of the dye with converted sp[2] to sp[3] carbon hybridization, and/or induce cleavage of the π–conjugation along the bridge while keeping the aromatic benzoindotricarbocyanine moieties intact. The observation that NETs were somewhat more susceptible to photo-degradation than free ICG (Figures 4b and S4) suggests that entrapment of ICG within the NETs may weaken the alternating double bonds along the polyene bridge, and/or alter its electronic localization and polarizability, a proposition consistent with the excitonic theory described earlier. Our results are in agreement with those reported by Holzer *et al.* where there were progressively increased optical transmissions (i.e., lower absorption) through various solvents (e.g., H$_2$O, D$_2$O, human plasma) containing

free ICG as the laser irradiation time increased[31]. For example, these investigators reported nearly 12% increase in transmission of 785 nm light through a sample containing 10 μM ICG dissolved in H_2O after 600 s of photo-irradiation at this wavelength and $I_o = 0.17$ mW·cm^{-2}; transmission subsequently increased to about 25% after 2,400 s of irradiation[31].

The major potential advantages of NETs as compared to other types of dye-loaded nano-constructs are their safety, and longevity within the circulation. As constructs that can be engineered autologously, NETs offer the potential of being biodegradable, and non-immunogenic photo-theranostic platforms for use in personalized nanomedicine. Flower *et al.* reported no immune or allergic responses, even after multiple injections of ICG-loaded EGs into monkeys and rabbits despite the fact human-derived erythrocytes were used to fabricate the constructs[28].

The natural lifetime of erythrocytes in systemic circulation is on the order of 90–120 days. While further studies are needed to determine the biodistribution and vascular retention time of NETs, the reported circulation times of erythrocytes-based carrier systems exceed those of synthetic vectors, which are on the order of several hours (e.g., <10 hours for polyethylene glycol-liposomes with diameters in the range of 50–500 nm)[19]. Hu *et al.*, investigated the circulation dynamics of nano-constructs (≈80 nm diameter) composed of a poly (lactic-co-glycolic acid) core coated with erythrocyte-derived membranes in mice[32]. The investigators reported that the constructs were retained in blood for three days with circulation half-life of nearly 40 hours[21,32].

In a clinical study, patients with acute lymphoblastic leukemia (ALL) were injected with erythrocytes encapsulating L-asparaginase (L-ASNase) to treat ALL. L-ASNase loaded erythrocytes were still detectable within the vasculature at 24 days following the first injection[33]. As compared to non-encapsulated L-ASNase, the investigators reported a reduction in the number and severity of allergic reactions in those patients receiving the L-ASNase loaded erythrocytes.

In another study, 20 patients with ulcerative colitis received autologously-derived erythrocytes encapsulating dexamethasone 21-P (Dex 21-P) as the therapeutic agent[34]. At 14 days post-infusion, there were still detectable levels of Dex 21-P within the plasma. There were no steroid-related adverse effects in patients treated with erythrocyte encapsulating Dex 21-P as compared to 8 of the 10 patients receiving oral steroids.

In summary, we have engineered a new type of optical nano-construct composed of erythrocyte-derived membranes encapsulating the organic NIR chromophore, ICG. To-date, only iron oxide nanoparticles are approved by the FDA for use in conjunction with MRI. There are currently no FDA-approved nano-constructs as contrast agents for use in optical imaging modalities, and furthermore, as a photo-theranostic material for combined optical imaging and photo-therapy. Given the existing FDA-approved status of ICG and prior clinical studies with erythrocytes-based delivery systems, NETs present a promising photo-theranostic candidate for clinical translation. For example, the enhanced permeability and retention effect in tumors may provide the basis for the delivery of NETs into tumors. Since particles with diameters <200 nm are more effective for extravasation into tumors[35], NETs may prove a suitable material for combined optical imaging and photothermal destruction of tumors. Other potential applications may include dynamic imaging and photo-destruction of vascular abnormalities, and longitudinal evaluations to assess therapeutic interventions.

Methods

Fabrication of NETs. The schematic of the NETs fabrication procedure is shown in Fig. S1 (Supplemental Information). We collected whole blood from mice through cardiac puncture using heparin coated tube and syringe. Whole blood was centrifuged at 800× g for five minutes at 4°C to separate the erythrocytes. The erythrocytes were then washed in 1 ml of cold 1× PBS (310 mOsm, pH = 8), and centrifuged at 800× g for five minutes at 4°C. Subsequently, 500 μl of packed erythrocytes were suspended

in one ml of hypotonic buffer (0.25×PBS buffer solution, 80 mOsm, pH = 8) and incubated at 4°C for 20 minutes. The erythrocytes were centrifuged at 800× g for five minutes at 4°C to separate the hemoglobin. The resulting erythrocyte ghosts (EGs) were sonicated in an ice bath sonicator at 60 W for five minutes. The EGs were extruded 20 times through 400 nm polycarbonate porous membranes, followed by 20 more extrusions through 100 nm polycarbonate porous membranes using an Avanti mini extruder.

To load ICG into the EGs, 300 μl of EGs suspended in PBS was incubated with 300 μl of ICG (500 μg/ml ≈ 0.65 mM) dissolved in PBS and 300 μl of hypotonic buffer (Na_2HPO_4/NaH_2PO_4, 140 mOsm, pH = 8) for five minutes at 4°C in dark. The suspension was then centrifuged, and washed twice at 14,000× g for 10 minutes at 4°C. The ICG-loaded EGs were re-suspended in cold 1×PBS buffer solution to restore tonicity.

Characterization of NETs. The hydrodynamic diameters of NETs suspended in PBS were measured by dynamic light scattering (Zetasizer NanoZS90, Malvern Instruments Ltd). To prepare samples for TEM, a drop of NETs suspension in PBS was placed on a carbon-coated grid for 10 minutes. The grid was rinsed twice with distilled water. To stain the NETs, a drop of 1% uranyl acetate solution was deposited on the grid and dried in air. The grid was imaged using a Philips TECNAI 12 Transmission Electron Microscope. The absorption spectra of NETs suspended in 2.4 ml of PBS were obtained using a UV-Visible spectrophotometer (Jasco-V670 UV-Vis spectrophotometer) with optical pathlength of 1 cm. The fluorescence spectra of NETs in response to 650 nm excitation with a 450 W xenon lamp were obtained using a fluorometer (Fluorolog-3 spectrofluorometer, Horiba Jobin Yvon). We obtained the normalized fluorescence spectra $\zeta(\lambda)$ as:

$$\zeta(\lambda) = \frac{F(\lambda)}{1 - 10^{-A(\lambda)}} \qquad (2)$$

where A and F are the wavelength-dependent absorbance, and intensity of the emitted fluorescent light, respectively.

Fluorescence microscopy imaging of human dermal microvascular endothelial (HDME) cells. To illustrate the effectiveness of NETs as photo-theranostic agents, we utilized HDME cells (ATCC®) as model cell systems for fluorescence imaging and photothermal destruction. We cultured the HDME cells in 96 well culture plates containing vascular cell basal medium supplemented with 5% Fatal Bovine Serum (FBS) and endothelial cell growth Kit-VEGF for 24 hours in advance of imaging to ensure adhesion and cell density growth to ≈10⁶ cells/ml. The cells were then incubated with complete vascular cell basal media containing NETs or 13 μM ICG (control) for three hours. We then washed the cells incubated with NETs or free ICG twice with PBS prior to imaging. The cells nuclei were stained using 4′,6-diamidino-2-phenylindole (DAPI). The fluorescence emission from DAPI in the range of 435–485 nm was collected in response to 360 ± 20 nm excitation. In response to photo-excitation by a Nikon Mercury/Xenon arc lamp providing light over the 740 ± 35 nm spectral band, the NIR emission (>770 nm) transmitted through a long pass filter was captured using an electron multiplier gained CCD camera (Quant EM- CCD, Hamamatsu) at integration time of 0.1 s and gain of 1.0.

Photothermal response and photostability of NETs, and photodestruction of HDME cells. To investigate the photothermal response of the NETs, we used a continuous wave near-infrared 808 nm diode laser with irradiation spot diameter of 2.2 mm, and incident irradiance (I_o) of 19.7 W/cm². NETs suspended in PBS, and ICG dissolved in PBS were prepared in concentrations that gave the same absorbance value at 808 nm for both samples. As the negative control sample, we irradiated the PBS solution at the same irradiation parameters as above. Same volume of each sample (120 μl) was irradiated, and temperature changes were measured using a negative temperature coefficient thermistor (20 kΩ, Vernier) connected to a Vernier LabQuest placed 2 mm outside the irradiation spot.

We investigated the photostability of the NETs by collecting their absorption spectra following laser irradiation of 120 μl of the NETs suspensions for various radiant exposure times (60, 90, 140, and 200 s) at 808 nm and $I_o = 19.7$ W/cm². Additionally, we performed a cyclic laser irradiation, and measured the resulting temperature response (Supplementary Information).

To investigate the photo-destructive capability of the NETs, we cultured the HDME cells in a 96 well-plate as described above. On the following day, cells were incubated with 200 μl of NETs suspended in PBS, or 200 μl (13 μM) of free ICG dissolved in PBS, in separate wells for three hours in dark at 37°C supplied with 5% CO_2. These levels of NETs or ICG were used to ensure the same absorbance value (0.6) at 808 nm in both NETs- and ICG-treated cells. Both the NETs- and ICG-treated cells were washed twice with PBS prior to laser irradiation experiments. We irradiated the cells incubated in PBS as negative control agent. Each well was irradiated at three different spots (each spot diameter = 2.2 mm), for 200 s. By using three spots, approximately 80% of the cells could be irradiated. Cells were stored for two hours post irradiation at 37°C supplied with 5% CO_2. The live/dead viability kit (L3224, Invitrogen) for mammalian cells was used to assess injury. Cell damage in each well was analyzed using a live/dead assessment kit for mammalian cells and a fluorescent microplate reader (Molecular Devices FlexStation II 384, Harlow Scientific). Specifically, live cells were identified using Calcein ($\lambda_{excitation}$ = 494 nm, $\lambda_{emission}$ = 517 nm) and dead cells using Ethidium homodimer-1 ($\lambda_{excitation}$ = 528 nm and $\lambda_{emission}$ = 617 nm).

Cytotoxicity assessment of NETs. To evaluate the potential cytotoxicity of the NETs, we cultured the HDEM cells in 96 well-plates as described above. On the following day, cells were washed with PBS and then incubated with complete cell culture media containing NETs for three and 24 hours. The effective dosage (D_{eff}) of the NETs for cytotoxicity experiments was 12 ml^{-1} where we define D_{eff} as the absorbance of the NETs population (1.2 at 808 nm) suspended in 100 µl of PBS solution. Cells incubated with complete cell culture media for 24 hours without any additional reagents were used as the positive control population. Cells incubated with 100 µl methanol for 24 hours were used as the negative control population. Cells were washed twice with PBS post incubation with NETs, and stained using the live/dead assay described above.

1. Pansare, V. J., Hejazi, S., Faenza, W. J. & Prud'homme, R. K. Review of long-wavelength optical and NIR imaging materials: contrast agents, fluorophores and multifunctional nano carriers. *Chem. Mater.* **13**, 812–827 (2012).
2. Fox, J. J. & Wood, E. H. Application of dilution curves recorded from the right side of the heart or venous circulation with the aid of a new indicator dye. *Proc. Mayo Clin.* **32**, 541 (1957).
3. Caesar, J., Sheldon, S., Cianduss, L., Guevara, L. & Sherlock, S. The use of indocyanine green in the measurement of hepatic blood flow and as a test for hepatic function. *Clin. Sci.* **21**, 43–57 (1961).
4. Yannuzzi, L. A. Indocyanine green angiography: A perspective on use in the clinical setting. *Am. J. Ophthalmol.* **151**, 745–751 (2011).
5. van der Vorst, J. R. *et al.* Dose optimization for near-infrared fluorescence sentinel lymph node mapping in patients with melanoma. *Br. J. Dermatol.* **168**, 93–98 (2013).
6. Jeschke, S. *et al.* Visualisation of the lymph node pathway in real time by laparoscopic radioisotope- and fluorescence-guided sentinel lymph node dissection in prostate cancer staging. *Urology* **80**, 1080–1086 (2012).
7. Crane, L. M. *et al.* Intraoperative near-infrared fluorescence imaging for sentinel lymph node detection in vulvar cancer: first clinical results. *Gynecol. Oncol.* **120**, 291–295 (2011).
8. Sevick-Muraca, E. M. *et al.* Imaging of lymph flow in breast cancer patients after microdose administration of a near-infrared fluorophore: Feasibility study. *Radiology* **246**, 731–741 (2008).
9. Smretschnig, E. *et al.* Half-fluence photodynamic therapy in chronic central serous chorioretinopathy. *Retina* **33**, 316–323 (2013).
10. Yannuzzi, L. A. *et al.* Indocyanine green angiography-guided photodynamic therapy for treatment of chronic central serous chorioretinopathy: a pilot study. 2003. *Retina* **Suppl. 1**, 288–298 (2012).
11. Costa, R. A. *et al.* Indocyanine green-mediated photothrombosis as a new technique of treatment for persistent central serous chorioretinopathy. *Curr. Eye Res.* **25**, 287–297 (2002).
12. Klein, A. *et al.* Indocyanine green-augmented diode laser treatment of port-wine stains: clinical and histological evidence for a new treatment option from a randomized controlled trial. *Br. J. Dermatol.* **167**, 333–342 (2012).
13. Liggett, P. E., Lavaque, A. J., Chaudhry, N. A., Jablon, E. P. & Quiroz-Mercado, H. Preliminary results of combined simultaneous transpupillary thermotherapy and ICG-based photodynamic therapy for choroidal melanoma. *Ophtalmic. Surg. Lasers Imaging* **36**, 463–470 (2005).
14. Yaseen, M. A., Yu, J., Wong, M. S. & Anvari, B. In-vivo fluorescence imaging of mammalian organs using charge-assembled mesocapsule constructs containing indocyanine green. *Opt. Express* **16**, 20577–20587 (2008).
15. Bahmani, B. *et al.* Effects of nano-encapsulation and PEGylation on biodistribution of indocyanine green in healthy mice: quantitative fluorescence imaging and analysis of organs. *Int. J. Nanomed.* **8**, 1609–1620 (2013).
16. Jung, B., Rao, A. L. & Anvari, B. Optical nano-constructs composed of genome-depleted brome mosaic virus doped with a near infrared chromophore for potential biomedical applications. *ACS Nano* **22**, 1243–1252 (2011).
17. Gupta, S. *et al.* Virus-mimicking nano-constructs as a contrast agent for near infrared photoacoustic imaging. *Nanoscale* **5**, 1772–1776 (2013).
18. Pierige, F., Serafini, S., Rossi, L. & Magnani, M. Cell-based drug delivery. *Adv. Drug Deliv. Rev.* **160**, 286–295 (2008).
19. Muzykantov, V. R. Drug delivery by red blood cells: vascular carriers designed by mother nature. *Expert. Opin. Drug Deliv.* **7**, 403–427 (2010).
20. Gutiérrez Millán, C., Colino Gandarillas, C. I., Sayalero Marinero, M. L. & Lanao, J. M. Cell-based drug delivery platforms. *Ther. Deliv.* **3**, 25–41 (2012).
21. Hu, C. M., Fang, R. H. & Zhang, L. Erythrocyte-inspired delivery systems. *Adv. Healthc. Mater.* **5**, 532–547 (2012).
22. Brahler, M. *et al.* Magnetite-loaded carrier erythrocytes as contrast agents for magnetic resonance imaging. *Nano Lett.* **6**, 2505–2509 (2006).
23. Chang, M. *et al.* Homologous RBC-derived vesicles as ultrasmall carriers of iron oxide for magnetic resonance imaging of stem cells. *Nanotechnology* **21**, 235103 (2010).
24. Antonelli, A., Sfara, C., Manuali, E., Bruce, I. J. & Magnani, M. Encapsulation of superparamagnetic nanoparticles into red blood cells as new carriers of MRI contrast agents. *Nanomedicine (Lond)* **6**, 211–223 (2011).
25. Ahn, S., Jung, S. Y., Seo, E. & Lee, S. J. Gold nanoparticle-incorporated human red blood cells (RBCs) for X-ray dynamic imaging. *Biomaterials* **32**, 7191–7199 (2011).
26. Milanick, M. A., Ritter, S. & Meissner, K. Engineering erythrocytes to be erythrosensors: first steps. *Blood Cells Mol. Dis.* **47**, 100–106 (2011).
27. Ritter, S. C., Milanic, M. A. & Meissner, K. E. Encapsulation of FITC to monitor extracellular pH: a step towards the development of red blood cells as circulating blood analyte biosensors. *Biomed. Opt. Express* **2**, 2012–2021 (2011).
28. Flower, R. *et al.* Observation of erythrocyte dynamics in the retinal capillaries and choriocapillaris using ICG-loaded erythrocyte ghost cells. *Invest. Ophthalmol. Vis. Sci.* **49**, 5510–5516 (2008).
29. Philip, R., Penzkofer, A., Baumler, W., Szeimies, R. M. & Abels, C. Absorption and fluorescence spectroscopic investigation of indocyanine green. *J. Photoch. Photbio. A* **96**, 137–148 (1996).
30. Kasha, M., Rawls, H. R. & Ashraf El-Bayoumi, M. The exciton model in molecular spectroscopy. *Pure Appl. Chem.* **11**, 371–392 (1965).
31. Holzer, W. *et al.* Photostability and thermal stability of indocyanine green. *J. Photochem. Photobiol. B.* **47**, 155–164 (1998).
32. Hu, C.-M. J. *et al.* Erythrocyte membrane-camouflaged polymeric nanoparticles as a biomimetic delivery platform. *Proc. Natl. Acad. Sci. U. S. A.* **108**, 10980–10985 (2011).
33. Domenech, C. *et al.* L-asparaginase loaded red blood cells in refractory or relapsing acute lymphoblastic leukaemia in children and adults: results of the GRASPALL 2005-01 randomized trial. *Br. J. Haematol.* **153**, 58–65 (2010).
34. Bossa, F. *et al.* Erythrocyte-mediated delivery of dexamethasone in patients with mild-to-moderate ulcerative colitis, refractory to mesalamine: a randomized, controlled study. *Am. J. Gastroenterol.* **103**, 2509–2516 (2008).
35. Peer, D. *et al.* Nanocarriers as an emerging platform for cancer therapy. *Nat. Nanotechnol.* **12**, 751–760 (2007).

Acknowledgements

Author contributions

B.A. conceived the project and the use of NETs as photo-theranostic agents; contributed to the design of the experiments, and interpretation of results and photophysics of NETs; wrote the main text of the manuscript with input provided by B.B; and guided the preparation of Figures. B.B. contributed to the design of the experiments, and interpretation of results; performed the experiments; prepared the Figures; wrote the Methods and Supplementary Information sections with guidance provided by B.A. D.B. contributed to fabrication of the NETs.

Additional information

Supplementary information accompanies this paper at http://www.nature.com/scientificreports

Competing financial interests: The authors declare no competing financial interests.

How to cite this article: Bahmani, B., Bacon, D. & Anvari, B. Erythrocyte-derived photo-theranostic agents: hybrid nano-vesicles containing indocyanine green for near infrared imaging and therapeutic applications. *Sci. Rep.* **3**, 2180; DOI:10.1038/srep02180 (2013).